

## Optimization of photoelectrochemical water splitting performance on hierarchical TiO<sub>2</sub> nanotube arrays†

Zhonghai Zhang and Peng Wang\*

Received 14th December 2011, Accepted 9th February 2012

DOI: 10.1039/c2ee03461a

In this paper, we show that by varying the voltages during two-step anodization the morphology of the hierarchical top-layer/bottom-tube TiO<sub>2</sub> (TiO<sub>2</sub> NTs) can be finely tuned between nanoring/nanotube, nanopore/nanotube, and nanohole–nanocave/nanotube morphologies. This allows us to optimize the photoelectrochemical (PEC) water splitting performance on the hierarchical TiO<sub>2</sub> NTs. The optimized photocurrent density and photoconversion efficiency in this study, occurring on the nanopore/nanotube TiO<sub>2</sub> NTs, were 1.59 mA cm<sup>−2</sup> at 1.23 V vs. RHE and 0.84% respectively, which are the highest values ever reported on pristine TiO<sub>2</sub> materials under illumination of AM 1.5G. Our findings contribute to further improvement of the energy conversion efficiency of TiO<sub>2</sub>-based devices.

### Introduction

Solar light is the most abundant energy source and the solar energy that strikes the earth in a day is more than the total energy consumption of the world in a year.<sup>1</sup> Solar energy collection, conversion and storage are three key processes for practical applications and these processes can all be integrated in a single monolithic photoelectrochemical (PEC) water splitting cell, within which the solar energy is converted and contained in the simplest chemical bond, H–H.<sup>2</sup> The PEC cells are typically designed with metal oxide semiconductors as photoelectrodes and noble metals as counter electrodes. Among the metal oxide semiconductors being intensively investigated (*e.g.*, TiO<sub>2</sub>,<sup>3,4</sup>

ZnO,<sup>5,6</sup> Fe<sub>2</sub>O<sub>3</sub>,<sup>7,8</sup> WO<sub>3</sub>,<sup>9</sup> and Cu<sub>2</sub>O<sup>10</sup>), TiO<sub>2</sub> distinguishes itself due to its favorable band-edge positions, superior chemical and optical stability, and low cost. However, due to two fundamental reasons, the photoconversion efficiency and photocurrent density of TiO<sub>2</sub> based photoanodes are still not satisfactory. First, the large band gap of TiO<sub>2</sub> (*i.e.*, 3.2 eV for anatase and 3.0 eV for rutile) limits its optical absorption within the UV light region; second, a general mismatch between the optical path length required for high light absorption (at least 1 μm for 90% light absorption) and the optimal charge diffusion length (usually 70 nm for the minority carrier: hole) leads to fast photoelectron–hole recombination in powder TiO<sub>2</sub> based PEC cells.<sup>11–13</sup> Sensitization with small band gap semiconductors/dyes and non-metal doping are among the most investigated approaches for expanding the TiO<sub>2</sub> optical absorption spectrum into the visible and infrared regions.<sup>14</sup> Due to the high level of control over their aspect ratio, one-dimensional nanostructures of semiconductors, such as nanotubes (NTs), nanorods, and nanowires, permit optimization of the optical path length and

Chemical and Life Science and Engineering Division, Water Desalination and Reuse Center, King Abdullah University of Science and Technology, Thuwal 23955-6900, Saudi Arabia. E-mail: peng.wang@kaust.edu.sa

† Electronic Supplementary Information (ESI) available: Extra SEM images, crystallite sizes data and open circuit potential vs. time profile. See DOI: 10.1039/c2ee03461a

### Broader content

The present annual worldwide energy consumption is ~15 TW and is expected to reach 30 TW by 2050. Moreover, due to stock limitation, energy supply from non-renewable fossil fuels, such as oil, coal, natural gas, is shrinking. In view of this, generation of clean and renewable energy has drawn significant interest from academia and industry. Solar light is without any doubt the most renewable energy source available to us. The collection, conversion and storage of solar energy are three key processes for practical applications and these processes can all be integrated in a single monolithic photoelectrochemical (PEC) water splitting cell. Within it the solar energy is converted and contained in hydrogen gas, which is considered as “new oil” in the future. In this study, hierarchical TiO<sub>2</sub> nanotube (TiO<sub>2</sub> NT) arrays, widely regarded as promising candidates for enhancing solar energy efficiency in PEC cells, were prepared by two-step anodization for PEC water splitting applications. We show that simple, controllable, and rational modulation of morphology, optical absorption and crystallinity of the hierarchical TiO<sub>2</sub> NTs can remarkably boost their water splitting performance. Our findings contribute to further improvement of the energy conversion efficiency of TiO<sub>2</sub>-based devices.



charge diffusion length relatively independently and they are thus regarded as promising candidates to solve the issue of mismatch between optical path and charge diffusion lengths.<sup>15,16</sup> In particular, TiO<sub>2</sub> NTs arrays prepared in anodization processes have recently attracted considerable research attention owing to their facile preparation procedure, high surface area for contact with the supporting electrolyte, high light harvesting efficiency enhanced by light scattering, and high electron mobility induced by their one-dimensional nanostructure.<sup>17,18</sup> Normally, TiO<sub>2</sub> NTs fabricated in conventional one-step anodization processes suffer from disparity in tube lengths and considerable tube array surface roughness. A two-step anodization process, which is composed of the first anodization for growth of TiO<sub>2</sub> NTs and their subsequent removal and the second anodization to grow TiO<sub>2</sub> NTs from the same substrate, is an alternative for the preparation of much more uniform TiO<sub>2</sub> NT arrays.<sup>19,20</sup> Moreover, under suitable synthesis conditions, unique hierarchical top-layer/bottom-tube TiO<sub>2</sub> NT arrays can be fabricated, which have been proven to possess significantly better performance in dye sensitized solar cells than those fabricated using the conventional one-step anodization.<sup>21</sup> Furthermore, it is possible that with suitable morphology, the top-layer can serve as a photonic crystal to enhance the optical absorption of the hierarchical TiO<sub>2</sub> NTs. However, there are only a few reports available in the literature examining PEC performances with hierarchical TiO<sub>2</sub> NTs based photoelectrodes.<sup>22,23</sup>

The objective of this study is to optimize the PEC water splitting performance of the hierarchical top-layer/bottom-tube TiO<sub>2</sub> NTs photoanodes, which can be achieved by adjusting the voltages applied in the two anodization steps (Scheme 1). The key contribution of the present study is that we show by applying a simple fabrication strategy the photocurrent density and

photoconversion efficiency of the hierarchical TiO<sub>2</sub> NTs can be remarkably boosted. As a matter of fact, the optimal photocurrent density and photoconversion efficiency of the hierarchical TiO<sub>2</sub> NTs in our system were 1.59 mA cm<sup>-2</sup> and 0.84%, the highest values ever reported for single component TiO<sub>2</sub> materials.

## Experimental

### Chemicals and materials

A 2 mm thick titanium sheet (99.6%, Strem Chemicals) was cut into pieces of 25 × 10 mm<sup>2</sup>. Ethylene glycol (EG), ammonia fluoride (NH<sub>4</sub>F), potassium hydroxide (KOH) were purchased from Acros Organics and used as received. All aqueous solutions were prepared using deionized (DI) water with a resistivity of 18.2 MΩ cm that was prepared by a Millipore system.

### Preparation of TiO<sub>2</sub> NTs

The TiO<sub>2</sub> NTs were fabricated by a two-step anodization process. Prior to anodization, the Ti sheets were first degreased by sonicating in ethanol and room-temperature DI water, followed by drying in a pure nitrogen stream. The anodization was carried out using a conventional two-electrode system with the Ti sheet as an anode and a Pt gauze (Aldrich, 100 mesh) as a cathode. All electrolytes consisted of 0.5 wt% NH<sub>4</sub>F in EG solution with 2 vol% water. All anodizations were carried out at room temperature. In the first-step anodization, the Ti sheet was anodized at 60, 80, or 100 V for 60 min, and then the as-grown nanotube layer was ultrasonically removed in DI water. The same Ti sheet then underwent the second anodization at different potentials in range of 20–100 V with tunable duration to control the thickness of the NTs. After the two-step anodization, the prepared TiO<sub>2</sub> NT samples were cleaned with DI water and dried with N<sub>2</sub> gas. The anodized TiO<sub>2</sub> NTs were annealed in air at 450 °C for 1 h with a heating rate of 5 °C min<sup>-1</sup>.

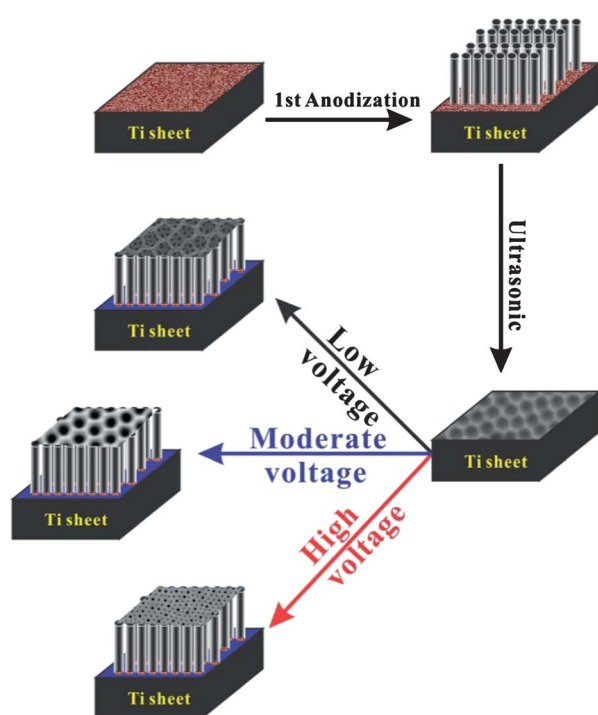
### Characterization of TiO<sub>2</sub> NTs

The morphology of the hierarchical TiO<sub>2</sub> NTs was determined by field-emission scanning electron microscope (FESEM, FEI Quanta 600). The crystalline structure was analyzed by X-ray diffraction (XRD, Bruker D8 Discover diffractometer, using Cu Kα radiation, λ = 1.540598 Å). The diffuse reflectance UV–vis adsorption spectra were recorded on spectrophotometer (Shimadzu, UV 2550), with fine BaSO<sub>4</sub> powder as a reference.

### Photoelectrochemical characterization of TiO<sub>2</sub> NTs

The photoelectrochemical performance of the TiO<sub>2</sub> NTs was evaluated using a three-electrode configuration with a TiO<sub>2</sub> NTs electrode, Ag/AgCl electrode, and Pt mesh as the working, reference and counter electrode, respectively. The supporting electrolyte was 1 M KOH solution. The potential and photocurrent of the photoelectrode were controlled by a potentiostat and were reported against the reversible hydrogen electrode (RHE) following the equation below:

$$E_{\text{RHE}} = E_{\text{Ag/AgCl}} + 0.059\text{pH} + E^{\circ}_{\text{Ag/AgCl}} \text{ with } E^{\circ}_{\text{Ag/AgCl}} = 0.1976 \text{ V at } 25^{\circ}\text{C} \quad (1)$$



**Scheme 1** Two-step anodization synthesis of the hierarchical TiO<sub>2</sub> NTs.



The scan rate for the linear sweep voltammetry was  $5 \text{ mV s}^{-1}$ . The photoresponse was evaluated under chopped light irradiation (light on/off cycles: 60 s) at a fixed electrode potential of 1.23 V vs. RHE. The photocurrent was measured under irradiation from a 300 W Xe lamp (PLS-SXE300, PE300BF). The intensity of the light source was calibrated with a Si diode (Model 818, Newport) to simulate AM 1.5 illumination ( $100 \text{ mW cm}^{-2}$ ). The electrochemical impedance spectra (EIS) were measured using a PGSTAT302N Autolab Potentiostat/Galvanostat (Metrohm) equipped with a frequency analyzer module (FRA2) with an excitation signal of 10 mV amplitude. The impedance vs. frequency spectra were acquired at the open circular potential of the system under the illumination conditions. Afterward, impedance vs. potential measurements at a fixed frequency were performed to determine the carrier density.

## Results and discussion

As shown in Scheme 1, to prepare the hierarchical  $\text{TiO}_2$  NTs, a Ti sheet was first anodized under certain voltage to grow  $\text{TiO}_2$  NTs on its surface. The  $\text{TiO}_2$  NTs (Fig. S1a, ESI†) were subsequently removed by ultrasonication, leaving behind on the Ti sheet surface a regular hexagonally packed round concave morphology (Fig. 1d4, Fig. S1b, ESI†). The patterned Ti sheet was

then subject to the second anodization to yield uniform  $\text{TiO}_2$  NTs with unique hierarchical top-layer/bottom-tube nanostructures. It is generally believed that the growth of porous or tubular anodic metal oxide films, such as alumina and titania, is an outcome of the competition between the electric field driven oxidation of metal ( $v_{\text{electro}}$ ) to form oxides, and the electric field assisted and chemical dissolution of the metal oxide layer ( $v_{\text{dis}}$ ).<sup>24</sup> With the existence of fluoride anions as electrolytes in the hierarchical  $\text{TiO}_2$  NT synthesis system, the dissolution of titania in the form of  $[\text{TiF}_6]^{2-}$  is greatly affected by the applied electric field. Thus, it is reasonable to believe that the density of the electric field applied during anodization significantly affects the morphology of the hierarchical  $\text{TiO}_2$  NT arrays. In this study three different voltages (*i.e.*, 60, 80, or 100 V) were applied in the first anodization step for fast patterning of the sheet and convenient removal of the tubes by ultrasonication, and five voltages (*i.e.*, 20, 40, 60, 80, 100V) were employed in the second anodization step. The samples were denoted by S-*x*-*y* with *x* and *y* being the anodization voltage in the first and second anodization steps respectively.

Fig. 1a through 1e present scanning electron microscopy (SEM) images of the hierarchical  $\text{TiO}_2$  NTs prepared at different voltages in the second anodization, with the first anodization voltage fixed at 60 V. We denote the morphology of the hierarchical  $\text{TiO}_2$  NTs samples synthesized at 20 and 40 V (*i.e.*, S-60-20 and S-60-40) as nanoring/nanotube and that at 60, 80 and 100 V (*i.e.*, S-60-60, S-60-80, and S-60-100) as nanopore/nanotube (Fig. 1). With increasing density of the applied electric field,  $v_{\text{electro}}$  increases, whereas  $v_{\text{dis}}$  decreases due to coulomb force on the  $[\text{TiF}_6]^{2-}$  anion. Thus, at the low voltages of 20 and 40 V in the second anodization, and presumably due to the relatively high  $v_{\text{dis}}$ , relatively little accumulation/deposition of  $\text{Ti}(\text{OH})_4$  occurred at the openings of the NTs where the NTs met the bulk electrolyte, resulting in the formation of the unique nanoring/nanotube hierarchical nanostructures (*i.e.*, S-60-20 and S-60-40) (Fig. 1a–b). As the anodization voltage increases further, accumulation/deposition of  $\text{Ti}(\text{OH})_4$  at the entrance of the NTs increases correspondingly. This leads to the sequential formation of nanopore and nanohole top structures, with the diameters of the openings decreasing with increasing voltages. On the other hand, as an increase in  $v_{\text{electro}}$  favors the formation of a thicker oxide layer, at high anodization voltages the applied electric field tends to preferentially focus on the bottom of the concavity generated in the first-step anodization where the electrical resistance is the lowest. As a result, the diameters of the bottom tubes of S-60-60, S-60-80, and S-60-100 increase with increasing voltages, which agrees well with the literature.<sup>25,26</sup> To investigate the effect of the voltage in the first anodization step, S-60-80 was compared with S-80-80 and S-100-80. As shown in Fig. 1f and 1g, S-80-80 revealed similar nanopore/nanotube structures to S-60-100 whereas S-100-80 exhibited a unique top morphology, which is denoted as a nanohole–nanocave/nanotube structure. As clearly shown in Fig. 1g, the top of the nanohole–nanocave/nanotube structure consists of holes with a pore size of around 50 nm and concaves with closed bottoms. The distinctly different morphology of S-100-80 may be due to the formation of a thick oxide barrier layer in the first anodization step at the high voltage (*i.e.*, 100 V). As shown in the insets in Fig. 1, all samples were precisely controlled with a uniform length of  $\text{TiO}_2$  NTs in the

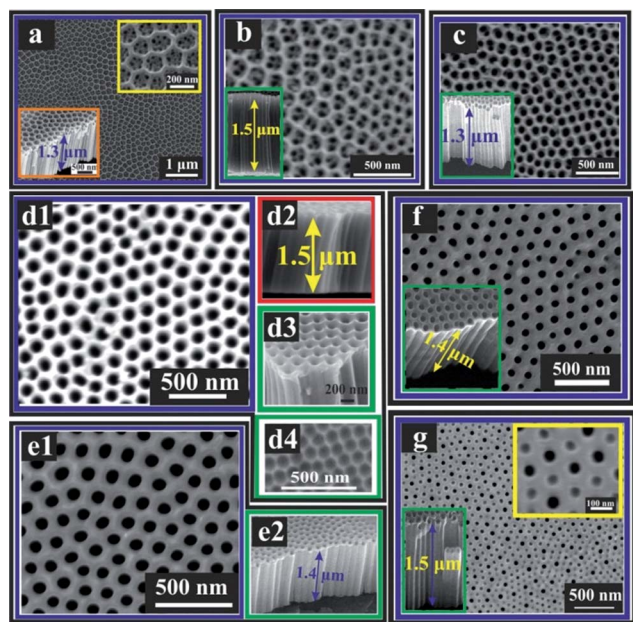


**Fig. 1** SEM images of (a) S-60-20; top right inset shows a high magnification image and bottom left inset shows cross-sectional view with a length of the  $\text{TiO}_2$  NTs of 1.3  $\mu\text{m}$ ; (b) S-60-40; inset shows cross-sectional view with a length of 1.5  $\mu\text{m}$ ; (c) S-60-60; inset shows cross-sectional view with a length of 1.3  $\mu\text{m}$ ; (d1) S-60-80; (d2) cross-sectional view of S-60-80 with a length of 1.5  $\mu\text{m}$ , (d3) 15° cross-sectional view of S-60-80; (d4) regular hexagonally packed pattern with round concave morphology on a Ti sheet surface after ultrasonic removal of the NTs layer; (e1) S-60-100; (e2) cross-sectional view of S-60-100 with a length of 1.4  $\mu\text{m}$ ; (f) S-80-80; inset shows cross-sectional view with a length of 1.4  $\mu\text{m}$ ; (g) S-100-80; top right inset shows high magnification image, and bottom left inset shows cross-sectional view with a length of 1.5  $\mu\text{m}$ .





range of 1.3–1.5  $\mu\text{m}$ , for the purpose of minimizing the effect of tube length disparity on PEC performance.

Linear sweep photovoltammetry measurements were performed to determine the photocurrent densities of different samples using a three-electrode electrochemical system in a 1 M KOH electrolyte under AM 1.5G (100  $\text{mW cm}^{-2}$ ) illumination. Analysis of the photocurrent densities on different samples (Fig. 2a) allows us to draw the following three major conclusions.

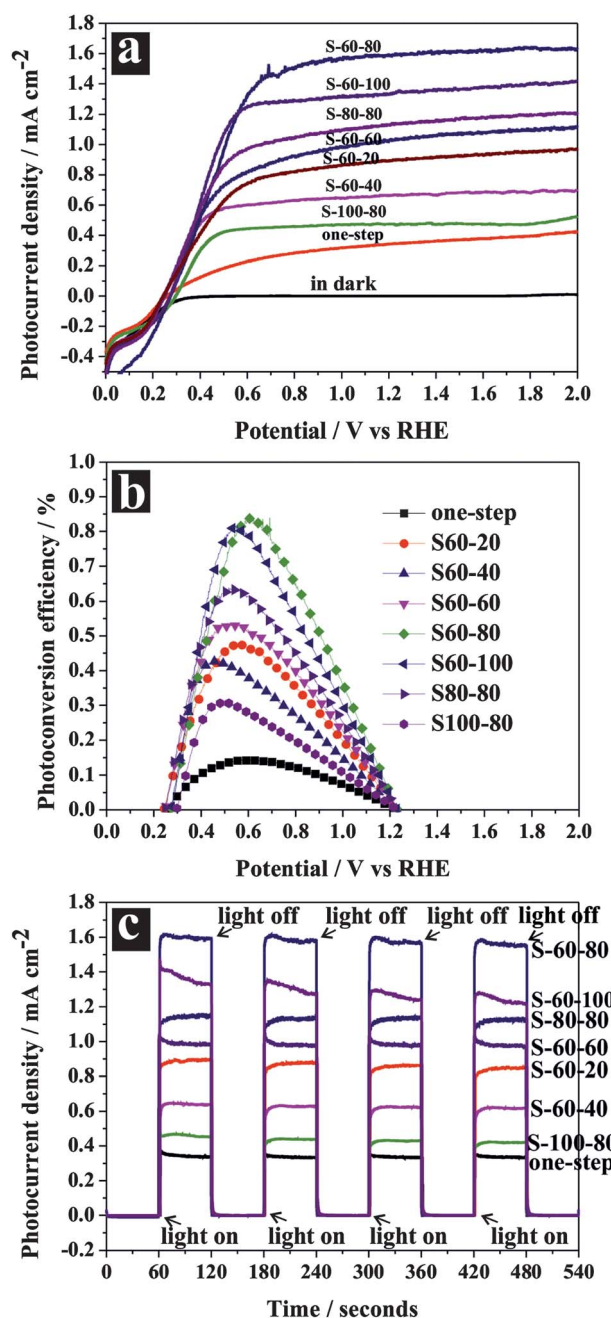


**Fig. 2** Photoelectrochemical properties of hierarchical  $\text{TiO}_2$  NTs electrodes: (a) linear-sweep voltammograms collected with a scan rate of 5  $\text{mV s}^{-1}$  in the dark and under illumination; (b) photoconversion efficiency as a function of the applied potential; (c) amperometric  $I-t$  curves at an applied potential of 1.23 V vs. RHE under illumination with 60 s light on/off cycles.

(1) All samples prepared by the two-step anodization method showed consistently higher photocurrent densities under the same conditions (Fig. 2a) than ones prepared by the conventional one-step method (anodization with 80 V), implying that the hierarchical  $\text{TiO}_2$  nanostructures favor better PEC performances. The photocurrent density of the  $\text{TiO}_2$  NTs photoanode prepared by the conventional one-step anodization method was only 0.345  $\text{mA cm}^{-2}$  at 0.23 V vs. Ag/AgCl or 1.23 V vs. RHE, which is the potential often chosen as a metric to evaluate the performance of photoanodes as it corresponds to the water oxidation potential. S-60-80, among all samples, generated the highest photocurrent density of 1.59  $\text{mA cm}^{-2}$  at the same potential, which is also the highest photocurrent density value ever reported on pristine  $\text{TiO}_2$  materials under illumination of AM 1.5G. It is worth mentioning that it is not our intention to compare the PEC water splitting performance of our system (*i.e.*, single-component  $\text{TiO}_2$ ) with those involving extra chemical addition/modifications (*e.g.*, ion intercalation, hydrogenation, noble metal deposition, sensitization). (2) The photocurrent densities ( $I$ ) of different samples showed a general order of  $I_{\text{nanopore/nanotube}} > I_{\text{nanoring/nanotube}} > I_{\text{nanohole-nanocave/nanotube}}$ . The nanohole-nanocave/nanotube sample (*i.e.*, S-100-80) showed a relatively low photocurrent density (0.480  $\text{mA cm}^{-2}$ ), supposedly due to the closed nanocave structures on its surface which effectively blocks the light absorption and solution infiltration. On the other hand, the nanopore/nanotube samples (*i.e.*, S-60-60, S-60-80, and S-60-100) showed higher photocurrent densities than the nanoring/nanotube samples (*i.e.*, S-60-20 and S-60-40), which is due to the formers' better degree of crystallinity and high optical absorption (to be discussed in a later section). (3) Among all of the nanopore/nanotube samples, S-60-80, the one with improved uniformity, showed the highest photocurrent density, which is due to its better optical absorption. In addition, a uniform morphology reduces structure defects which would otherwise serve as photoelectron/hole recombination centers, and thus favors high PEC performance. The photoconversion (*i.e.*, photon-to-hydrogen) efficiency of the hierarchical  $\text{TiO}_2$  samples was calculated using the following equation:<sup>27</sup>

$$\eta (\%) = I(E_{\text{rev}}^{\circ} - V)/J_{\text{light}} \quad (2)$$

where  $\eta$  is the photoconversion efficiency,  $I$  is the photocurrent density ( $\text{mA cm}^{-2}$ ),  $J_{\text{light}}$  is the incident light irradiance ( $\text{mW cm}^{-2}$ ),  $E_{\text{rev}}^{\circ}$  is the standard reversible potential which is 1.23 V vs. RHE, and  $V$  is the applied bias potential vs. RHE. Fig. 2b presents the plots of the photoconversion efficiency vs. applied bias potentials. Among all of the samples, the  $\text{TiO}_2$  NTs photoanode prepared by the conventional one-step anodization method showed the lowest optimal photoconversion efficiency of 0.15% while S-60-80 exhibited the highest optimal photoconversion efficiency of 0.84%, which, to our best knowledge, is also the highest photoconversion efficiency of pristine  $\text{TiO}_2$  materials ever reported under illumination of AM 1.5G. The photoconversion efficiency of all two-step samples were all greater than 0.31%, at least two times higher than that of the one-step sample. The photocurrent densities and photoconversion efficiencies of all samples are summarized in Table 1. Amperometric  $I-t$  measurements were also performed to examine the photoresponse of the hierarchical  $\text{TiO}_2$  NTs over time (Fig. 2c),



**Table 1** Summary of PEC performance of hierarchical TiO<sub>2</sub> NTs

Samples	Current density at 1.23 V vs. RHE/mA cm <sup>-2</sup>	Photoconversion efficiency (%)	Carrier density/cm <sup>-3</sup>
One-step	0.342	0.15	$2.45 \times 10^{19}$
S-60-20	0.901	0.48	$3.57 \times 10^{19}$
S-60-40	0.670	0.43	$3.02 \times 10^{19}$
S-60-60	1.03	0.54	$4.69 \times 10^{19}$
S-60-80	1.59	0.84	$8.48 \times 10^{19}$
S-60-100	1.34	0.81	$5.84 \times 10^{19}$
S-80-80	1.14	0.64	$5.81 \times 10^{19}$
S-100-80	0.480	0.32	$2.72 \times 10^{19}$

and fast photoresponses were recorded for all samples under conditions of alternating light on and light off and this photocurrent pattern was highly reproducible for many on/off cycles.

Optical absorption and crystalline properties are two important factors for the PEC performance on TiO<sub>2</sub> materials. A material with a better optical absorption and higher crystallinity will subsequently result in a better PEC performance. Therefore, diffuse reflectance UV-vis absorption spectra and XRD measurement were employed in this study to characterize the optical absorption properties and crystallinity of the hierarchical TiO<sub>2</sub> NTs (Fig. 3). As shown in Fig. 3a (DRS UV-vis absorption spectra), all two-step hierarchical TiO<sub>2</sub> NTs samples depicted better UV absorption than one-step TiO<sub>2</sub> NTs sample due to their unique hierarchical nanostructures and also better morphological uniformity. A better surface morphological uniformity might indicate better periodicity of the photonic

crystals formed by the top porous layers and thus a better optical absorption. Among the hierarchical TiO<sub>2</sub> NT samples, those with better surface morphological uniformity, such as S-60-20, S-60-80, S-80-80, presented better optical absorption.

The XRD patterns of the hierarchical TiO<sub>2</sub> NTs after annealing in the same conditions (450 °C for 1 h in air) were shown in Fig. 3b. Clearly, all hierarchical TiO<sub>2</sub> NTs samples formed pure crystalline anatase and showed a strong preferential orientation of (101). The average crystallite size of the samples was estimated using the Debye-Scherrer equation from the (101) crystal planes,<sup>28</sup> and was used as a criterion to evaluate the degree of crystallinity of the samples (Fig. S2, ESI†). As is generally accepted, the crystallite size of TiO<sub>2</sub> NTs increases with increasing voltages employed in anodization process.<sup>29</sup> This can be explained by the fact that high voltage favors the formation of bigger crystal nucleus and thus results in a better crystallinity and less defects, with which our results agree well. In our case, with a fixed first anodization voltage of 60 V, at the second anodization voltages of 20, 40, 60, 80 and 100 V, the average crystallite size was 28, 29, 31, 34, and 43 nm respectively, increasing monotonically (Fig. S2, ESI†).

By comparing optical absorption properties and crystallinity of the hierarchical TiO<sub>2</sub> NTs against their PEC performances (Fig. 2), we conclude that the optimal optical absorption properties and crystallinity of the hierarchical TiO<sub>2</sub> NTs cannot be achieved simultaneously. For example, S-60-20 did not show a high photocurrent density even though it had a good optical absorbance in the UV region because its low crystallinity was the limiting factor; S-60-100 failed to generate the highest photocurrent density even though it possessed the best crystallinity among all of the samples because its relatively low optical absorbance limited its performance in this case. Among all samples, S-60-80 showed the highest PEC performance, which was due to a suitable combination of its good light absorption and crystallinity.

To better understand the enhanced PEC performance, the inherent electronic properties of the hierarchical TiO<sub>2</sub> NTs were characterized by measuring their open-circuit photovoltage decay (OCPVD) and electrochemical impedance spectra (EIS). OCPVD was measured to assess photoelectron lifetime in this study and thus to evaluate the recombination rate of the photoelectrons and holes. OCPVD measurement consists of turning off illumination at a steady state and monitoring the subsequent decay of photovoltage,  $V_{oc}$ , with time (Fig. S3). The  $V_{oc}$  decay rate is directly related to the photoelectron lifetime by the following equation:<sup>30</sup>

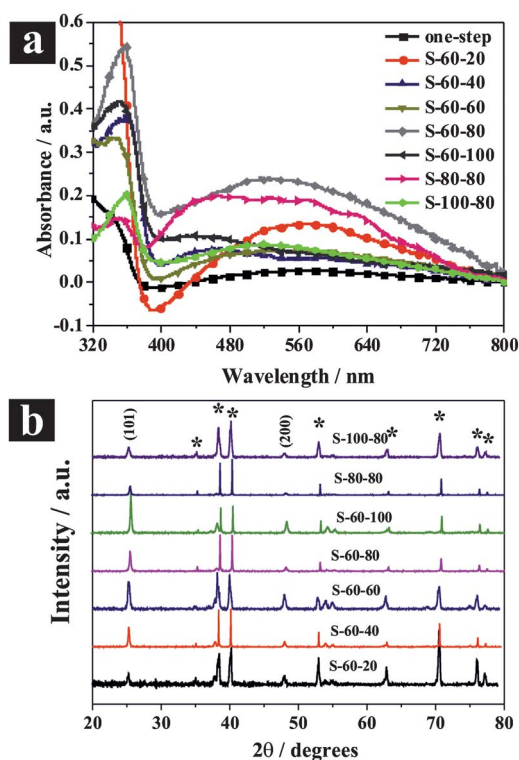


**Fig. 3** (a) Diffuse reflectance UV-vis absorption spectra of the hierarchical TiO<sub>2</sub> NTs. (b) XRD patterns of the hierarchical TiO<sub>2</sub> NTs (the asterisk denotes Ti patterns).



$$\tau = \frac{k_B T}{e} \left( \frac{dV_{oc}}{dt} \right)^{-1} \quad (3)$$

where  $\tau$  is the potential dependent photoelectron lifetime,  $k_B$  is Boltzmann's constant,  $T$  is the temperature,  $e$  is the charge of a single electron, and  $V_{oc}$  is the open-circuit voltage at time  $t$ . The calculated photoelectron lifetime is shown in Fig. 4 as a function of  $V_{oc}$ . Clearly, the photoelectron lifetime increases with decreasing  $V_{oc}$ . The nanopore/nanotube samples (*i.e.*, S-80-80, S-60-80, S-60-100) showed relatively long electron lifetime, contributing to their high PEC performances.

EIS is a powerful tool for studying the interfacial properties between electrodes and solutions. The EIS measurements were carried out covering the frequency range of  $10^5$ –0.1 Hz using an amplitude of 10 mV at the open circuit potential of the system. Fig. 5a presents Nyquist plots for different hierarchical TiO<sub>2</sub> NTs photoanodes under illumination. Semicircles in the Nyquist plots convey information on charge transfer process as the diameters of the semicircles are equal to charge transfer resistance of a sample. As depicted in Fig. 5a, the semicircular diameters for the nanopore/nanotube samples are much smaller than others, and S-60-80 shows the smallest arch diameter among all samples, indicating that the nanopore/nanotube samples possess smaller charge transfer resistance and thus better electron mobility. The capacitance measurement on the electrode/electrolyte was conducted at 5 kHz to determine carrier density ( $N_D$ ) of the TiO<sub>2</sub> NTs based electrodes following the equation below:<sup>31</sup>

$$\frac{1}{C^2} = \frac{2}{N_D e \epsilon_0 \epsilon} \left[ (U_s - U_{FB}) - \frac{k_B T}{e} \right] \quad (4)$$

where  $C$  is the space charge capacitance in the semiconductor;  $N_D$  is the electron carrier density;  $e$  is the elemental charge value;  $\epsilon_0$  is the permittivity of a vacuum;  $\epsilon$  is the relative permittivity of the semiconductor;  $U_s$  is the applied potential;  $T$  is the temperature; and  $k_B$  is the Boltzmann constant. Fig. 5b presents the Mott–Schottky (MS) plot as  $1/C^2$  vs. potential. The slopes of the linear parts of the curves in the MS plot are positive, indicating n-type semiconductors. The carrier density  $N_D$  was determined from Fig. 5b using the following equation:<sup>31</sup>

$$N_D = - \left( \frac{2}{e \epsilon \epsilon_0} \right) \left( \frac{d(1/C^2)}{d(U_s)} \right)^{-1} \quad (5)$$

Using  $e = 1.6 \times 10^{19}$ ,  $\epsilon_0 = 8.86 \times 10^{-12}$  F m<sup>-1</sup>, and  $\epsilon = 48$  for anatase TiO<sub>2</sub>,<sup>32</sup> the carrier densities were calculated and summarized in Table 1. Among all of the samples, S-60-80 showed the highest carrier density of  $8.48 \times 10^{19}$  cm<sup>-3</sup>. An increase in the  $N_D$  value improves the charge transport in semiconductors and it can also shift the Fermi level of the semiconductors toward its conduction band, which further facilitates the charge separation at the semiconductor/electrolyte interface. The enhanced charge separation and charge transport are favorable to PEC performance enhancement.

## Conclusion

In summary, the two-step anodization is an effective strategy for the preparation of hierarchical TiO<sub>2</sub> NTs. By tuning the voltages used in the anodization processes, morphology, optical absorption and crystallinity can be altered, which allow us to optimize the PEC water splitting performance on these TiO<sub>2</sub> NTs photoelectrodes. The optimal photocurrent density and photo-conversion efficiency in our system are 1.59 mA cm<sup>-2</sup> and 0.84% under illumination of AM 1.5G (100 mW cm<sup>-2</sup>), the highest values ever reported for single component TiO<sub>2</sub> materials. This result points out the possibility of further improving performance in not only PEC systems, but also in solar cells and other photocatalytic fields and thus contributes to high energy conversion devices.

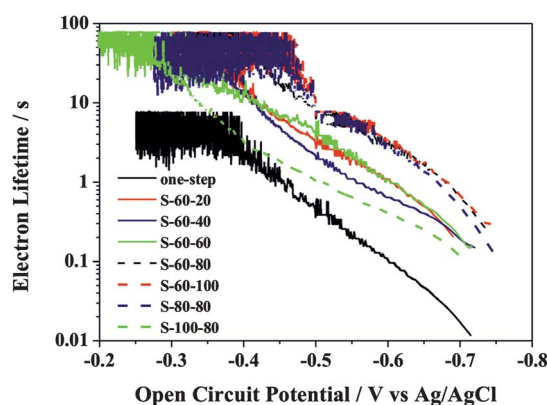


**Fig. 4** Electron lifetime measurements determined from the decay of open circuit potential in dark.

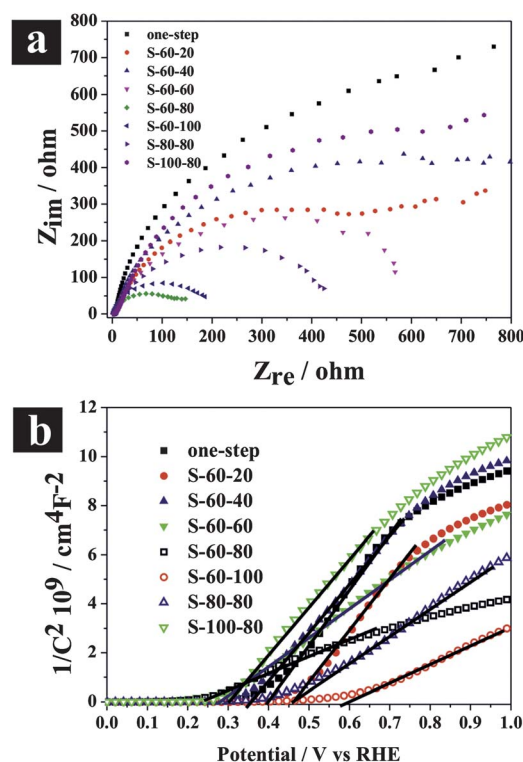


**Fig. 5** (a) Electrochemical impedance spectra of Nyquist plots ( $Z_{re}$  vs.  $Z_{im}$ ), and (b) Mott–Schottky plot at a fixed frequency of 5 kHz on hierarchical TiO<sub>2</sub> NTs photoanodes.

## Notes and references

- 1 N. S. Lewis, *Science*, 2007, **315**, 798–801.
- 2 M. G. Walter, E. L. Warren, J. R. McKone, S. W. Boettcher, Q. Mi, E. A. Santori and N. S. Lewis, *Chem. Rev.*, 2010, **110**, 6446–6473.
- 3 N. K. Allam, C. W. Yen, R. D. Near and M. A. Ei-Sayed, *Energy Environ. Sci.*, 2011, **4**, 2909–2914.
- 4 P. Roy, C. Das, K. Lee, R. Hahn, T. Ruff, M. Moll and P. Schmuki, *J. Am. Chem. Soc.*, 2011, **133**, 5629–5631.
- 5 X. Yang, A. Wolcott, G. Wang, A. Sobo, R. C. Fitzmorris, F. Qian, J. Z. Zhang and Y. Li, *Nano Lett.*, 2009, **9**, 2331–2336.
- 6 A. Wolcott, W. A. Smith, T. R. Kuykendall, Y. Zhao and J. Z. Zhang, *Adv. Funct. Mater.*, 2009, **19**, 1849–1856.
- 7 K. Sivula, R. Zboril, F. L. Formal, R. Robert, A. Weidenkaff, J. Tucek, J. Frydrych and M. Grätzel, *J. Am. Chem. Soc.*, 2010, **132**, 7436–7444.
- 8 D. K. Zhong, M. Cornuz, K. Sivula, M. Grätzel and D. R. Gamelin, *Energy Environ. Sci.*, 2011, **4**, 1759–1764.
- 9 V. Cristino, S. Caramori, R. Argazzi, L. Meda, G. L. Marra and C. A. Bignozzi, *Langmuir*, 2011, **27**, 7276–7284.
- 10 A. Paracchino, V. Laporte, K. Sivula, M. Grätzel and E. Thimsen, *Nat. Mater.*, 2011, **10**, 456–461.
- 11 M. Liu, N. de Leon Snapp and H. Park, *Chem. Sci.*, 2011, **2**, 80–87.
- 12 H. Tang, K. Prasad, R. Sanjines, P. E. Schmid and F. Levy, *J. Appl. Phys.*, 1994, **75**, 2042–2047.
- 13 M. Takahashi, K. Tsukigi, T. Uchino and T. Yoko, *Thin Solid Films*, 2001, **388**, 231–236.
- 14 X. Chen, S. Shen, L. Guo and S. S. Mao, *Chem. Rev.*, 2010, **110**, 6503–6570.
- 15 A. Wolcott, W. A. Smith, T. R. Kuykendall, Y. Zhao and J. Z. Zhang, *Small*, 2009, **5**, 104–111.
- 16 X. Feng, K. Shankar, O. K. Varghese, M. Paulose, T. J. Latempa and C. A. Grimes, *Nano Lett.*, 2008, **8**, 3781–3786.
- 17 H. E. Prakasam, K. Shankar, M. Paulose, O. K. Varghese and C. A. Grimes, *J. Phys. Chem. C*, 2007, **111**, 7235–7241.
- 18 P. Roy, S. Berger and P. Schmuki, *Angew. Chem., Int. Ed.*, 2011, **50**, 2904–2939.
- 19 S. Li, G. Zhang, D. Guo, L. Yu and W. Zhang, *J. Phys. Chem. C*, 2009, **113**, 12759–12765.
- 20 D. Wang, B. Yu, C. Wang, F. Zhou and W. Liu, *Adv. Mater.*, 2009, **21**, 1964–1967.
- 21 M. Ye, X. Xin, C. Lin and Z. Lin, *Nano Lett.*, 2011, **11**, 3214–3220.
- 22 Z. H. Zhang, M. F. Hossain and T. Takahashi, *Int. J. Hydrogen Energy*, 2010, **35**, 8528–8535.
- 23 F. Wang, Y. Liu, W. Dong and Z. Kang, *J. Phys. Chem. C*, 2011, **115**, 14635–14640.
- 24 J. Yan and F. Zhou, *J. Mater. Chem.*, 2011, **21**, 9406–9418.
- 25 J. Park, S. Bauer, K. von der Mark and P. Schmuki, *Nano Lett.*, 2007, **7**, 1686–1691.
- 26 J. M. Macak, H. Tsuchiya and P. Schmuki, *Angew. Chem., Int. Ed.*, 2005, **44**, 2100–2102.
- 27 G. Wang, H. Wang, Y. Ling, Y. Tang, X. Yang, R. C. Fitzmorris, C. Wang, J. Z. Zhang and Y. Li, *Nano Lett.*, 2011, **11**, 3026–3033.
- 28 B. D. Cullity, *Elements of X-ray diffraction*. 2nd ed. Reading, MA: Addison-Wesley; 1978. pp. 283.
- 29 N. K. Allam and C. A. Grimes, *Langmuir*, 2009, **25**, 7234–7240.
- 30 B. H. Meekins and P. V. Kamat, *ACS Nano*, 2009, **3**, 3437–3446.
- 31 G. Wang, Q. Wang, W. Lu and J. Li, *J. Phys. Chem. B*, 2006, **110**, 22029–22034.
- 32 P. K. Ghosh and M. E. Azimi, *IEEE Trans. Dielectr. Electr. Insul.*, 1994, **1**, 975–981.

